



Cite this: *Phys. Chem. Chem. Phys.*,
2017, **19**, 27478

Periodic DFT+*U* investigation of the bulk and surface properties of marcasite (FeS₂)

Nelson Y. Dzade  ^{*a} and Nora H. de Leeuw  ^{*ab}

Marcasite FeS₂ and its surface properties have been investigated by Hubbard-corrected Density Functional Theory (DFT+*U*) calculations. The calculated structural parameters, interatomic bond distances, elastic constants and electronic properties of the bulk mineral were determined and compared with earlier theoretical reports and experimental data where available. We have also investigated the relative stabilities, interlayer spacing relaxations, work functions, and electronic structures of the {010}, {101}, {110} and {130} surfaces under dehydrated and hydrated conditions. Using the calculated surface energies, we have derived the equilibrium crystal shape of marcasite from a Wulff construction. The {101} and {010} surfaces dominate the marcasite crystallite surface area under both dehydrated and hydrated conditions, in agreement with their relative stabilities compared to the other surfaces. The simulated scanning tunneling microscopy (STM) images of the {101} and {010} facets are also presented, for comparison with future experiments.

Received 30th June 2017,
Accepted 14th September 2017

DOI: 10.1039/c7cp04413e

rsc.li/pccp

1. Introduction

Iron sulfide minerals are abundant in nature and exist in a variety of phases with stoichiometries that range from the sulfur-deficient mackinawite FeS_{1-x} through iron-deficient pyrrhotite Fe_{1-x}S to greigite (Fe₃S₄) and pyrite (FeS₂).¹ Iron disulfide (FeS₂) occurs naturally as two polymorphs; pyrite (p-FeS₂) crystallizes in the cubic space group, *Pa3* while marcasite (m-FeS₂) belongs to orthorhombic *Pnnm*.² Iron pyrite has received much attention as a promising photovoltaic material because of its suitable band gap ($E_g = 0.95$ eV), high abundance, nontoxicity, and strong light absorption ($\sim 10^5$ cm⁻¹ for $h\nu > 1.3$ – 1.4).^{3–12}

Marcasite, the lesser known polymorph, is often considered to be an undesired contaminant phase for photovoltaic applications,^{13,14} because of its reported small band gap of 0.34 eV.¹⁵ Wadia and co-workers have speculated that the presence of trace amounts of marcasite in pyrite would significantly lower the band gap and therefore deteriorate the material's photovoltaic performance.^{13,14} However, recently published studies have thrown doubt on the earlier reported band gap of 0.34 eV for marcasite.^{16–21} Theoretical investigations have predicted that marcasite should have a band gap that is quite similar to that of pyrite (around 0.8–1.1 eV),^{16–20} whereas recent diffuse reflectance spectroscopy (DRS) measurements of natural marcasite samples have estimated the optical absorption gap to be

approximately 0.83 ± 0.02 eV,²¹ which is similar to the band gap of pyrite (0.95 eV).¹¹ These recent findings suggest that marcasite, which co-exists with pyrite and was originally regarded as a detrimental impurity, may actually be a highly useful semi-conductor and photocatalyst in its own right.

The development of an efficient photo-catalyst, however, requires an atomic-level understanding of the structure and composition, as well as information about the relative stabilities of its major surfaces as they dictate its morphology and reactivity towards adsorbing species.^{22–24} Detailed information regarding the structure, electronic and mechanical stability of the bulk material is also required. In earlier studies, the phase stability and thermoelectric properties of the naturally occurring marcasite phase of FeS₂ under ambient conditions has been investigated using first-principles calculations.^{18,25} Total energy calculations show that marcasite FeS₂ was stable at ambient conditions, and that it undergoes a first-order phase transition to pyrite FeS₂ at around 3.7–5.4 GPa at 0 K.^{18,25} Reich and Becker have also employed first-principles and Monte Carlo calculations to investigate the thermodynamic mixing properties of arsenic into bulk pyrite and marcasite.²⁶ From their calculated enthalpies, configurational entropies and Gibbs free energies of mixing, it was shown that the two-phase mixtures of FeS₂ (pyrite or marcasite) and FeAsS (arsenopyrite) are energetically more favorable than the solid solution Fe(S,As)₂ (arsenian pyrite or marcasite) for a wide range of geologically relevant temperatures.²⁶ There also exists significant information in the literature on the oxidation and chemistry of different stoichiometric and defective pyrite surfaces using *ab initio* theoretical calculations^{27–31} and experimental^{32–34} investigations. Hydration and early oxidation

^a Department of Earth Sciences, Utrecht University, Princetonplein 9, 3584 CC, Utrecht, The Netherlands. E-mail: N.Y.Dzade@uu.nl

^b School of Chemistry, Cardiff University, Main Building, Park Place, CF10 3AT, Cardiff, UK. E-mail: deLeeuwN@cardiff.ac.uk

of the surfaces of mackinawite,^{35,36} greigite,^{37,38} and violarite (FeNi_2S_4)³⁹ have also been investigated using DFT calculations. However, to date, no systematic theoretical study has been conducted to investigate the structures and stabilities of the major surfaces of marcasite, which makes this investigation timely.

In this study, we have employed Density Functional Theory calculations, with Hubbard corrections for the electron correlation in the localized d-Fe orbitals (DFT+ U), to first investigate the structures, electronic and mechanical properties of bulk marcasite. Secondly, the composition and structure, as well as the relative stabilities of the major surfaces of marcasite have been characterized systematically under dehydrated and hydrated conditions. The electronic properties of each surface, including the work function (Φ) have also been determined and are discussed. Using the calculated surface energies, we have derived the equilibrium morphology of marcasite crystals using Wulff construction.⁴⁰ Finally, we have used the HIVE program⁴¹ to simulate the topographical Scanning tunneling microscopy (STM) images of the $\{101\}$ and $\{010\}$ surfaces, which are the dominant growth facets expressed in the marcasite crystal morphology.

2. Computational details

The optimized structures were determined using plane-wave density functional theory (PW-DFT) calculations within the Vienna Ab initio Simulation Package (VASP code).^{42–45} The interactions between the valence electrons and the ionic core were described with the projected augmented wave (PAW) method^{43,46} and the electronic exchange–correlation potential was calculated using the Perdew–Burke–Ernzerhof (PBE) generalized gradient approximation (GGA) functional,^{47,48} with Hubbard U correction (PBE+ U).^{49–51} The + U correction term provides an accurate treatment of the electron correlation in the localized d-Fe orbitals, which is crucial for a proper description of the structural and electronic properties of these materials. We have used an effective U of 2 eV, which has been shown to give an accurate description of the structural parameters and the electronic properties of pyrite and marcasite FeS_2 .^{16,20,52–54} Van der Waals dispersion forces were accounted for in all calculations through the Grimme DFT-D3 functional,⁵⁵ which adds a semi-empirical dispersion potential to the conventional Kohn–Sham DFT energy as implemented in the VASP code. A plane-wave basis set with a kinetic energy cutoff of 500 eV was tested to be sufficient to converge the total energy of the FeS_2 to within 10^{-6} eV and the residual Hellman–Feynman forces in the ionic relaxations were converged to within 10^{-3} eV \AA^{-1} . The Brillouin zone was sampled using a $9 \times 9 \times 9$ mesh of Monkhorst–Pack k -points.⁵⁶ A higher k -points mesh of $13 \times 13 \times 13$ was used to determine the electronic structures of marcasite. For the surface calculations, the k -meshes were chosen in such a way that a similar spacing of points in the reciprocal space was maintained.

The elastic stiffness constants were calculated by the stress–strain method.^{57–61} The strain imposed on the crystals is set as follows: $\varepsilon = \varepsilon_1, \varepsilon_2, \varepsilon_3, \varepsilon_4, \varepsilon_5$, and ε_6 , where $\varepsilon_1, \varepsilon_2, \varepsilon_3$ are the normal strains and $\varepsilon_4, \varepsilon_5, \varepsilon_6$ are the shear strains. The corresponding

stresses ($\sigma = \sigma_1, \sigma_2, \sigma_3, \sigma_4, \sigma_5, \sigma_6$) for the deformed crystals due to each set of applied strains can be calculated from first-principles. According to Hooke's Law, the relationship between strain and stress is $\sigma_i = C_{ij}\varepsilon_j$, where C_{ij} are the elastic stiffness constants, which can be presented in a 6×6 matrix. In the case of a cubic system, there are only three independent elastic constants, *i.e.*, C_{11}, C_{12} , and C_{44} ; whereas for an orthorhombic system, as in marcasite, the number of independent elastic constants increases to nine, *i.e.*, $C_{11}, C_{22}, C_{33}, C_{12}, C_{13}, C_{23}, C_{44}, C_{55}$, and C_{66} . The derived elastic constants are useful in predicting the structural stability of materials: the bulk modulus (B_V) measures the material's resistance to uniform compression, whereas the shear modulus (G_V) measures the material's response to shearing strains. The bulk modulus (B_V) and shear modulus (G_V) of marcasite were estimated using the Voigt approximation.^{62,63} According to the Voigt (V) bounds for orthorhombic structures, the bulk and shear moduli in terms of elastic stiffness coefficient elements C_{ij} 's can be simplified as follows:

$$B_V = \frac{1}{9}(C_{11} + C_{22} + C_{33}) + \frac{2}{9}(C_{12} + C_{13} + C_{23}) \quad (1)$$

$$G_V = \frac{1}{15}(C_{11} + C_{22} + C_{33} - C_{12} - C_{13} - C_{23}) + \frac{1}{5}(C_{44} + C_{55} + C_{66}) \quad (2)$$

The Young's modulus (E) and Poisson's ratio (ν), which are characteristic properties of a material, related to its elasticity, and are often used to provide a measure of the stiffness of a solid, were obtained by the following formulas:

$$E = \frac{9BG}{(3B + G)}, \quad \nu = \frac{(3B - 2G)}{2(3B + G)} \quad (3)$$

The major surface structures of marcasite were created from the relaxed bulk material using the METADISE code,⁶⁴ which ensures the creation of surfaces with zero dipole moment perpendicular to the surface plane.⁶⁵ For each surface, the slab thickness, of at least 10 \AA , was increased until convergence of the surface energy was achieved within 1 meV per cell. In each simulation cell, a vacuum region of 15 \AA was tested to be sufficient to avoid interactions between periodic slabs. From a full geometry relaxation of the ionic positions of each surface in order to incorporate surface relaxation effects, we have computed the surface energy (γ), which is the energy required to cleave an infinite crystal in two—*i.e.*, the amount of energy required to create a new surface. This is a difficult quantity to determine experimentally because it usually requires measuring surface tension at the melting temperature of the material.⁶⁶ Theoretical determination of this quantity is, however, relatively easy and it is particularly useful in studies of the relative stability of different surface facets, with a low positive value indicating a stable surface.⁶⁷ The relative stabilities of the marcasite surfaces were determined according to their relaxed surface energy (γ_r), calculated as:

$$\gamma_r = \frac{E_{\text{slab}}^{\text{relaxed}} - nE_{\text{bulk}}}{2A} \quad (4)$$

where $E_{\text{slab}}^{\text{relaxed}}$ is the energy of the relaxed slab, nE_{bulk} is the energy of an equal number (n) of the bulk FeS atoms, A is the area of the slab surface and the factor of 2 reflects the fact that there are two surfaces for each slab, which have identical atomic ordering at the bottom and top layers. Because of the presence of water in the environment, we have also calculated the surface energies of the surfaces with a monolayer of adsorbed water at both sides of the slabs, where we considered that a monolayer was obtained when all surface cation sites were terminated by a water molecule. The surface energy of the hydrated surfaces was calculated as follows:

$$\gamma_{\text{hydrated}} = \frac{E_{\text{slab+water}}^{\text{relaxed}} - mE_{\text{water}} - nE_{\text{bulk}}}{2A} \quad (5)$$

where $E_{\text{slab+water}}^{\text{relaxed}}$ is the energy of the surface with adsorbed water and mE_{water} is the total energy of an equivalent number of water molecules (m) in the liquid phase which helps to assess the stability of the surface in an aqueous environment. The energy of liquid water is the sum of the self-energy of water due to the intra-molecular forces, and the energy of condensation due to the intermolecular forces (-44 kJ mol^{-1} at 25°C).⁶⁸ To characterize the strength of water adsorption and to determine whether or not successful adsorption had occurred on each surface, we have calculated the energies of adsorption (E_{ads}) using eqn (6).

$$E_{\text{ads}} = \frac{1}{m} [E_{\text{surface+m(water)}} - (E_{\text{surface}} + mE_{\text{water}})] \quad (6)$$

where $E_{\text{surface+m(water)}}$ and E_{surface} represent the total energy of the water-FeS₂ system and the clean FeS₂ surface, respectively. By this definition, a negative value of E_{ads} corresponds to an exothermic and favourable adsorption process. The multilayer relaxations for the hydrated surface (Δd_{ij}) were calculated as the percentage difference in the surface interlayer spacing, $d_{ij\text{-hydrated}}$, from the layer spacing of the same orientation in the geometry of the unrelaxed surface structure, $d_{ij\text{-unrelaxed}}$, created from the equilibrium bulk material. In these simulations, since the surface model is constructed from the optimized bulk structure, the required surface layer spacing is given by the spacing of the unrelaxed bulk-terminated slab structure.

$$\Delta d_{ij} = \frac{(d_{ij\text{-hydrated}} - d_{ij\text{-unrelaxed}})}{d_{ij\text{-unrelaxed}}} \times 100 \quad (7)$$

Within this definition, negative values correspond to inward relaxation (contraction) and positive values denote outward relaxation (dilation) of the interlayer spacings.

3. Results and discussions

3.1 Bulk properties

3.1.1 Structural parameters. Marcasite is the metastable dimorph of pyrite, and easily inverts to pyrite when heated in vacuum above about 400°C .⁶⁹ It is formed at low temperatures from acidic sulphidic aqueous fluids, and occurs mostly in near-surface deposits. Marcasite crystallizes in the orthorhombic structure (Fig. 1) with space group *Pnnm* (No. 58) and lattice

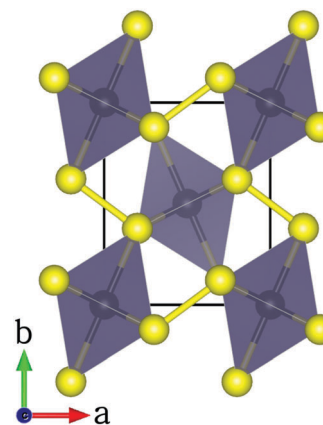


Fig. 1 The orthorhombic structure of marcasite FeS₂ in terms of FeS₆ octahedra. (Color scheme: Fe = grey, S = yellow.)

parameters $a = 4.436 \text{ \AA}$, $b = 5.414 \text{ \AA}$, $c = 3.381 \text{ \AA}$.^{2,70} Like pyrite, the marcasite structure can be described in terms of trigonally distorted FeS₆ octahedra and tetrahedrally coordinated sulfur atoms (Fig. 1).^{71–73} In the marcasite crystal structure, the FeS₆ units are edge-sharing along the unit cell *c*-axis and corner sharing in the other directions (Fig. 1). The Fe–S interactions in marcasite are made up of longer Fe–S bonds (2.253 \AA) and short Fe–S bonds (2.236 \AA) compared to the equivalent but longer Fe–S bonds of 2.263 \AA in pyrite.² Besides the FeS₆ octahedra, the marcasite structure is characterized by a rather short S–S interaction (2.212 \AA) which creates S₂ dumb-bell moieties.

Using the theoretical method described above and allowing all atoms to fully relax until the required accuracy was reached, we have determined the unit cell parameters of marcasite at $a = 4.405 \text{ \AA}$, $b = 5.404 \text{ \AA}$, $c = 3.382 \text{ \AA}$, which compares well with experimental data^{2,70} and a range of earlier theoretical values,^{16–18,25,26,74} reported in Table 1. The unit cell volume is also well reproduced in close agreement with reported experimental and theoretical data. Any differences found when compared to earlier theoretical results may be attributed to different parametrizations of the exchange–correlation functionals used in those calculations. The predicted interatomic distances (S–S = 2.190 \AA , longer Fe–S bonds = 2.246 \AA and shorter Fe–S bonds = 2.226 \AA) also show good agreement with experimental and theoretical data (Table 2).

3.2 Electronic properties

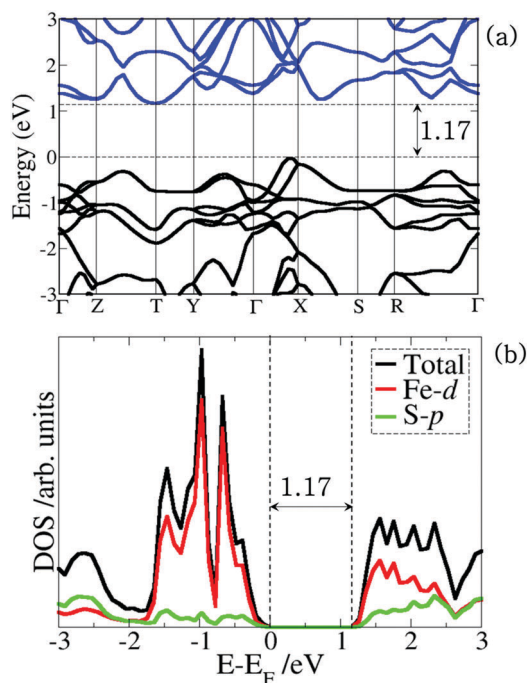
The electronic band structure of marcasite and the density of states projected on the Fe d-states and S p-states are shown

Table 1 Calculated lattice parameters of marcasite compared with previous theoretical and experimental results

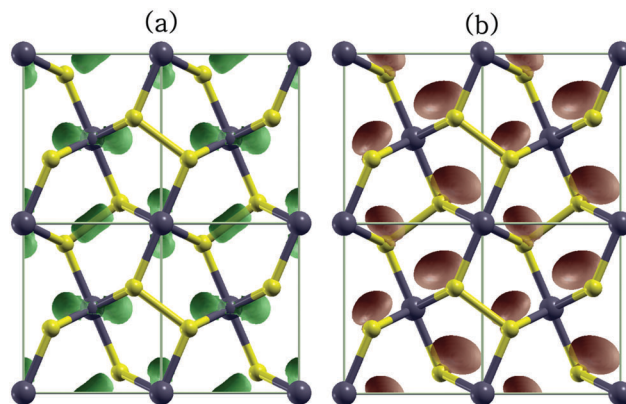
<i>a</i> (Å)	<i>b</i> (Å)	<i>c</i> (Å)	<i>V</i> (Å ³)	Investigation
4.436	5.414	3.381	81.20	Experiment (ref. 60)
4.405	5.404	3.382	80.51	This work
4.373	5.381	3.407	80.17	Calculation (ref. 64)
4.400	5.370	3.370	79.63	Calculation (ref. 26)
4.437	5.421	3.407	81.95	Calculation (ref. 16)
4.438	5.408	3.393	81.43	Calculation (ref. 25)
4.439	5.408	3.388	81.33	Calculation (ref. 18)

Table 2 Structural bonding distances in marcasite

$d(\text{Fe-S})$ (Å)	$d(\text{S-S})$ (Å)	$d(\text{Fe-Fe})$ (Å)	Investigation
2.210	2.190	3.360	Experiment (ref. 60)
2.236, 2.253	2.211	3.380	Experiment (ref. 2)
2.226, 2.246	2.190	3.382	This work
2.229	2.195	3.863	Calculation (ref. 64)
2.230	2.200	3.380	Calculation (ref. 18)

**Fig. 2** (a) Band structure along the high-symmetry directions of the Brillouin zone and (b) projected density of states (PDOS) of marcasite.

in Fig. 2. It is evident from the band structure (Fig. 2a) that marcasite is an indirect band gap semiconductor, because its conduction band minimum (CBM) and valence band maximum (VBM) are located at two different high-symmetry points in the Brillouin zone. The band gap is estimated to be 1.17 eV, which is in good agreement with earlier theoretical results of Sun *et al.*, (1.03 eV with PBE+*U*)¹⁶ and Schena *et al.*, (1.06 eV with GW approximation),¹⁷ respectively. The slightly larger band gap of marcasite compared to pyrite ($E_g = 0.95$)^{11,75} suggests that, contrary to earlier speculations,^{13,14} when present in trace amounts, marcasite is unlikely to undermine the photovoltaic performance of pyrite and it might actually be a useful semiconductor and photocatalyst in its own right. The projected density of states shown in Fig. 2b reveals that both the valence band and conduction band edges are composed mainly of the Fe 3d states with a small contribution of the S 3p states, indicating that marcasite is a Fe 3d \rightarrow Fe 3d charge transfer semiconductor, which agrees with earlier theoretical predictions.^{16,17} To determine the nature of the electronic states in the valence and conduction bands of marcasite, we have visualized the electronic wave functions of the highest occupied valence states and lowest unoccupied conduction states at the Γ point

**Fig. 3** Nature of electronic states (at the Γ point) of (a) the highest occupied valence band (HOVB) and (b) the lowest unoccupied conduction band (LUCB) of marcasite.

(see Fig. 3). It is clear that the lowest unoccupied conduction bands (LUCB) are comprised primarily of the p-states of sulfur, whereas the highest occupied valence bands (HOVB) are made up of the d-states of Fe and the p-states of S-S dimer interactions.

3.3 Mechanical properties

To determine the mechanical stability of marcasite, we have calculated its elastic properties. The elastic constants are fundamental parameters that describe the resistance of a material against applied mechanical deformation. Shown in Table 3 are the calculated single crystal elastic constants at the theoretical equilibrium volume. All the calculated single-crystal elastic constants satisfied the Born's mechanical stability criteria for orthorhombic structures,⁷⁶ thereby implying that the marcasite type FeS₂ is mechanically stable under ambient conditions. It is clear from the calculated elastic constants that $C_{22} > C_{33} > C_{11}$, which implies that marcasite is stiffer along the *b*-direction than along the *a*- and *c*-directions. Using the calculated elastic constants, we have obtained the bulk (*B*), shear (*G*), and Young's (*E*) moduli, and Poisson's ratio (ν) of marcasite (Table 3). The bulk modulus is calculated at 149.4 GPa, in very good agreement with the experimental value of 146.5 GPa⁷⁷ from

Table 3 Elastic stiffness constants (C_{ij}), bulk modulus (*B*), shear modulus (*G*), Young's modulus (*E*), and Poisson's ratio (ν) of marcasite at 0 GPa. Marcasite B_{expt} is 146.5 GPa⁶⁷

Parameter	Calc. (ref. 25)	Calc. (ref. 18)	This study
C_{11}	266	303.1	303.1
C_{22}	387	454.3	402.4
C_{33}	313	322.8	304.2
C_{44}	106	105.9	138.3
C_{55}	165	158.2	92.0
C_{66}	149	153.9	145.1
C_{12}	12	47.0	32.3
C_{13}	87	106.4	103.5
C_{23}	20	55.8	33.2
<i>B</i>	134	166.5	149.7
<i>G</i>	140	141.7	131.1
<i>E</i>	312	331.2	304.5
ν	0.1	0.2	0.2

the Birch–Murnaghan equation of state and the theoretical results of Gudelli *et al.*,¹⁸ Liu *et al.*,²⁵ and Sithole *et al.*⁷⁴ who reported 150.1, 145.9 and 152.22 GPa, respectively. The shear modulus is calculated to be 131.1 GPa, which is smaller than the bulk modulus, and therefore suggests that marcasite will be more prone to shear deformation than compressive deformation. The Poisson's ratio, which measures the stability of the crystal to shear and provides information about the interatomic forces in a given material, is calculated at 0.20 for marcasite. The small Poisson ratio calculated for marcasite (<0.25) indicates that the governing force in this material is covalent bonding,^{78,79} which arises from the hybridization of Fe d^2sp^3 orbitals and S sp^3 orbitals to form six Fe–S bonds and one S–S single bond per formula unit.^{80–82}

3.4 Surface properties

3.4.1 Surface structure and stability. We have used the relaxed structure of bulk marcasite to create the surfaces with the desired orientation, in order to eliminate the presence of fictitious forces during surface relaxation. The $\{010\}$, $\{101\}$, $\{110\}$ and $\{130\}$ planes are the dominant planes along which cleavage occurs in marcasite,^{83,84} and these planes are therefore the surfaces studied in this work. The $\{010\}$ surface is S-terminated, whereas the $\{101\}$, $\{110\}$ and $\{130\}$ surfaces can have more than one non-dipolar termination (either mainly S- or Fe-terminated based on height in the surface), all of which we have considered (Fig. 4–7). Because of water in the environment, the created surfaces were hydrated through adsorption of a monolayer of water at both sides of the slabs, where we considered that a monolayer of water was obtained when all surface cations had been terminated by water. The (a, b) dimensions of the (1×1) surface unit cells of the $\{101\}$, $\{010\}$, $\{110\}$ and $\{130\}$ surfaces

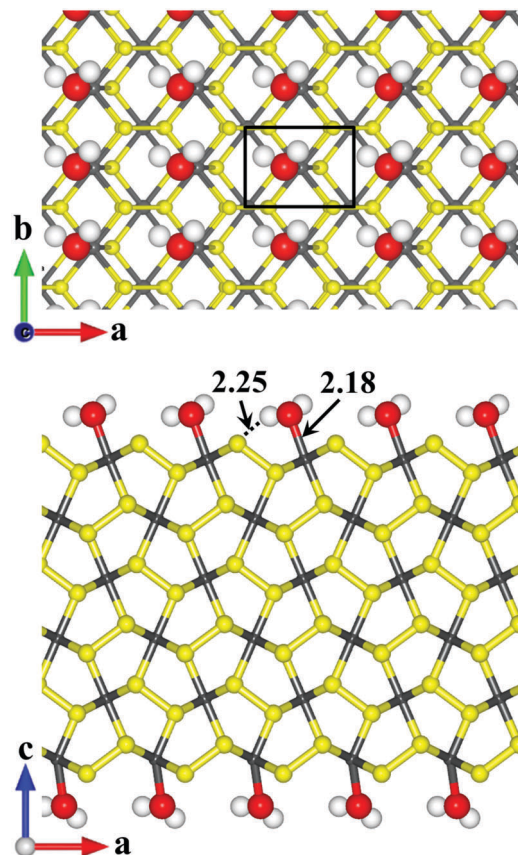


Fig. 5 Geometry-optimized structure of the hydrated $\text{FeS}_2\{010\}$ surface in top (top) and side (bottom) view. A (1×1) unit cell size is highlighted by a continuous line in the top view.

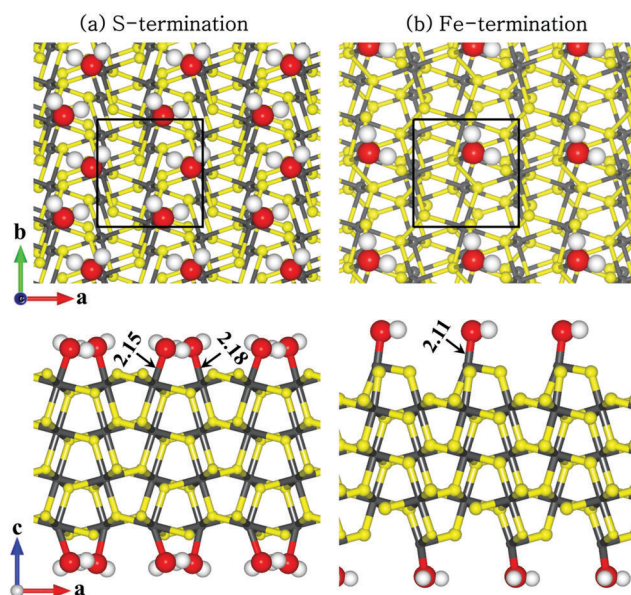


Fig. 4 Geometry-optimized structures of the hydrated $\text{FeS}_2\{101\}$ surface in top (top) and side (bottom) views. The sulfur termination is shown in (a) and iron termination in (b). A (1×1) unit cell size is highlighted by a continuous line in the top views.

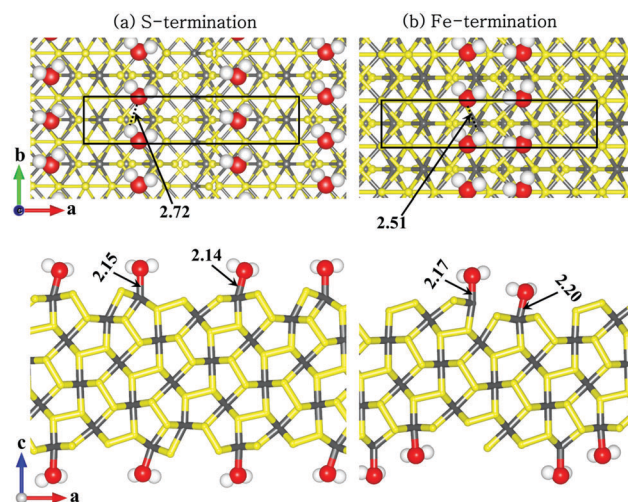


Fig. 6 Geometry-optimized structures of the hydrated $\text{FeS}_2\{130\}$ surface in top (top) and side (bottom) views. The sulfur termination is shown in (a) and iron termination in (b). A (1×1) unit cell size is highlighted by a continuous line in the top views.

are (5.404, 5.553 Å), (4.404, 3.382 Å), (3.382, 6.972 Å) and (3.382, 14.279 Å), respectively. As shown in the top views of the optimized adsorption structures, the $\{101\}$ -S and the $\{130\}$ -S/Fe surfaces

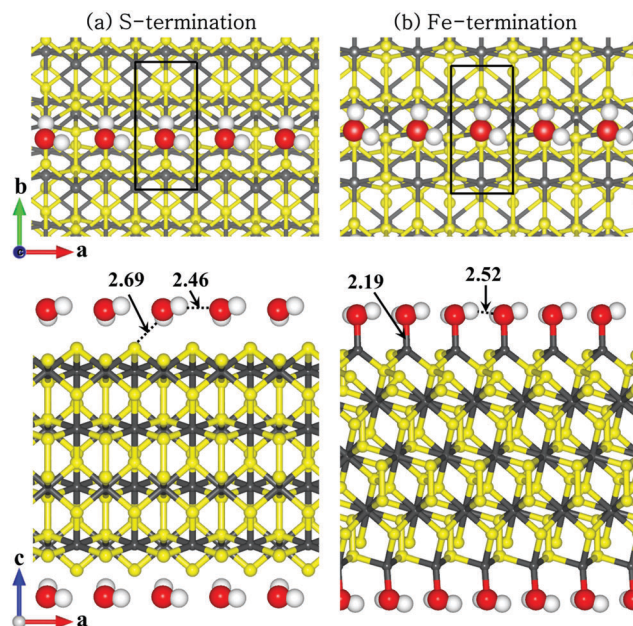


Fig. 7 Geometry-optimized structures of the hydrated $\text{FeS}_2\{110\}$ surface in top (top) and side (bottom) views. The sulfur termination is shown in (a) and iron termination in (b). A (1×1) unit cell size is highlighted by a continuous line in the top views.

were hydrated by two water molecules at each side of the (1×1) slabs, whereas the $\{010\}$ -S, $\{110\}$ -S/Fe surfaces were hydrated by one water molecule at each side of the (1×1) slabs. Due to the identical nature of the high symmetry adsorption sites in the periodic unit cells of each surface, the (1×1) cells were sufficiently large to investigate not only the interactions of the monolayers of water molecules with the surface, but also capture the hydrogen-bonded interactions between water molecules within and across periodic unit cells. We have computed structural relaxations and surface energies of the hydrated surfaces using larger supercells of each surface and found only small differences in the results compared to the (1×1) surface cells as shown in Table 4. From the calculated surface energies, we found that the mainly S-terminated surfaces were generally more stable than the Fe-terminations. The order of increasing surface energies, and therefore decreasing stability of the most stable S-terminated surfaces, before and after hydration is $\{101\} < \{010\} < \{130\} < \{110\}$. As is to be expected, hydration of the surfaces through adsorbed water molecules is found to

have a stabilizing effect on all the surfaces studied, since the adsorption acts to coordinate the water molecules to the under-coordinated Fe ions, thus providing a closer to bulk coordination of the surface species. The stabilization of the surfaces is reflected in the lower surface energies calculated for the hydrated surfaces compared to the dehydrated surfaces, as shown in Table 4. For example, the surface energies of the dehydrated $\{010\}$ and $\{101\}$ surfaces in S-terminations reduced by 47.1% and 53.5%, respectively. As shown in Table 4, the surface energies of the hydrated (1×1) and (2×2) unit cells of the $\{010\}$ surface with one and four water molecules, respectively, adsorbed at each side of the slabs, differ by only 0.03 J m^{-2} . Similarly, for a (2×2) unit cell of the $\{101\}$ surface with eight water molecules adsorbed at each side of the slab, the differences in surface energy relative to the (1×1) -S and (1×1) -Fe terminations, with two molecules adsorbed at each end of the slabs, are only 0.04 and 0.07 J m^{-2} , respectively. For the $\{110\}$ surface, the difference in the surface energy between the (1×1) and the (2×1) surfaces, with respectively one and two water molecules adsorbed at each side of the slabs, was calculated at 0.06 and 0.09 J m^{-2} for the S- and Fe-terminations, respectively. For the high index $\{130\}$ surface, the difference in surface energies between the (1×1) and (2×1) surfaces, with two and four water molecules, respectively, adsorbed at each end of the slabs, was calculated at 0.08 and 0.11 J m^{-2} for the S- and Fe-terminations, respectively. The small energy differences between the (1×1) cells and the larger cells containing more water molecules suggest that the (1×1) cells provide an adequate model for the simulation of marcasite surfaces hydrated by a monolayer of water.

On the $\{101\}$ surface (Fig. 4), the water molecules are coordinated by their oxygen ions to the surface Fe(II) ions at an average Fe–O distance of 2.165 \AA and 2.114 \AA at the S- and Fe-terminated surfaces, respectively. Consistent with their relative stability, the water molecule binds more strongly to the Fe-termination ($E_{\text{ads}} = -0.83 \text{ eV}$) than the S-termination ($E_{\text{ads}} = -0.49 \text{ eV}$). Similarly, on the $\{010\}$ surface (Fig. 5), the water molecules are coordinated by their oxygen ions to the surface Fe(II) ions at a distance of 2.184 \AA , releasing an adsorption energy of 1.10 eV . On the $\{130\}$ surface, the adsorption energies of water onto the S- and Fe-terminations were calculated at -0.83 eV and -0.95 eV , respectively, and the average Fe–O bond distances are calculated at 2.145 \AA and 2.185 \AA , respectively (Fig. 6). When adsorbed at the $\{110\}$ surface (Fig. 7), the water molecules released an adsorption energy of 0.37 eV at the S-terminated surface and 0.67 eV at the Fe-terminated surface. The weak adsorption of water on the S-terminated $\{110\}$ surface can be attributed to repulsive interactions between the O atom of the water molecules and the terminating S ions. Consistent with the weak adsorption of water on the S-terminated $\{110\}$ surface, the O–Fe distance is calculated at 3.645 \AA and the hydrogen atoms pointing towards the surface stand at 2.692 \AA away from the terminating S atoms. For the Fe-terminated $\{110\}$ surface, however, the water molecules are coordinated by their oxygen ions to surface Fe(II) ions at a distance of 2.186 \AA (Fig. 7). As commonly reported for other mineral surfaces,^{85–89} we found that the marcasite surfaces undergo only modest relaxations in

Table 4 Dehydrated (γ_r) and hydrated (γ_{hydrated}) surface energies of the (1×1) and larger $((2 \times 2)$ or (2×1)) (bracket values) surfaces of marcasite. The corresponding percentage relaxation after hydration is denoted as % relaxation

Surface	$\gamma_r (\text{J m}^{-2})$	$\gamma_{\text{hydrated}} (\text{J m}^{-2})$	% Relaxation
$\{010\}$ -S	1.53	0.81 (0.78)	47.1 (49.0)
$\{101\}$ -S	1.16	0.54 (0.50)	53.5 (56.9)
$\{101\}$ -Fe	2.30	1.85 (1.78)	19.6 (22.6)
$\{130\}$ -S	1.74	1.14 (1.06)	34.5 (39.1)
$\{130\}$ -Fe	2.04	1.45 (1.34)	28.9 (34.3)
$\{110\}$ -S	1.86	1.66 (1.60)	10.8 (13.9)
$\{110\}$ -Fe	2.67	2.21 (2.12)	17.2 (20.1)

Table 5 Percentage interlayer relaxations at hydrated marcasite surfaces. Positive and negative values denote dilation and contraction respectively

Surface	{010}		{101}		{110}		{130}	
Termination	S	S	Fe	Fe	S	Fe	S	Fe
Δd_{12}	+4.06	+5.32	-7.08	-6.07	-9.90	-5.36	-9.9	
Δd_{23}	-5.09	-3.77	+3.08	-3.27	+7.25	-4.07	+4.73	
Δd_{34}	+1.44	-1.23	+3.77	+5.75	-7.30	+7.92	+7.14	
Δd_{45}	-1.52	+3.71	-1.89	-6.66	+3.61	-4.93	+5.07	

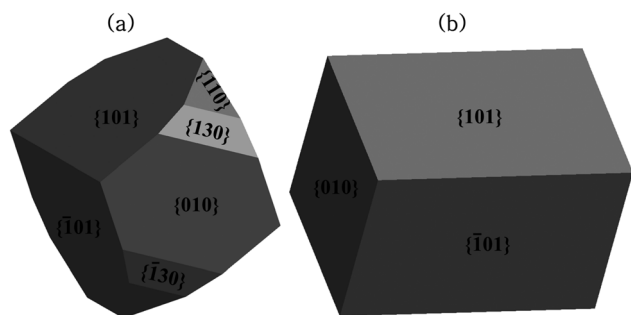


Fig. 8 Equilibrium morphology from Wulff construction of (a) the dehydrated and (b) the hydrated marcasite crystal.

their surface layers and interlayer spacings upon hydration, as shown in Table 5.

Following the procedure of the Wulff construction,⁴⁰ using the calculated surface energies (Table 4), we have constructed the equilibrium crystal morphology for marcasite under hydrated and dehydrated conditions, as shown in Fig. 8. We see that all four studied facets appear on the Wulff plot under dehydrated condition, with the facets corresponding to the {101} and {010} orientations enclosing the largest areas, in agreement with their surface stabilities. Hydration of the surfaces is, however, found to induce a faceting transformation (truncated octahedron \rightarrow rectangular), with only the {101} and {010} facets expressed in the hydrated equilibrium morphology (Fig. 8b), in agreement with their significant stabilization upon hydration compared to the other surfaces. Faceting transformation has been observed in crystals of other minerals^{90–94} and metals^{95–97} through the adsorption of small molecules, including water or an overlayer of surfactant molecules.

3.4.2 Simulation of scanning tunneling microscopy (STM) images. From the optimized structures of the S-terminated {101} and {010} surfaces, which are largely expressed in the equilibrium crystal morphology of marcasite under both hydrated and dehydrated conditions, we have derived their topographical STM images, which provide information about the spatial distribution of the valence band states in the vicinity of the Fermi energy (E_F). The STM images were simulated following the formulation in the Tersoff–Hamann approach,⁹⁸ where the STM tip was approximated to an infinitely small point source. The tunneling current between the surface and the tip in the STM experiments is proportional to the local density of states (LDOS) integrated between the Fermi energy and the sample bias. We have used the HIVE⁴¹ program for the production of

our STM topographic images, where the DFT-based partial charge density was integrated from -2.5 eV to the Fermi energy (E_F). In the constant current mode, the tip of the STM is moved across the surface where its height varies to keep the charge density at a constant value, which is given by a constant LDOS. The simulated STM images were mapped by means of the heights as a function of the position of the tip over the surface. More details about the method can be found elsewhere.⁹⁹ Due to the difficulty associated with obtaining single crystals with well-defined surfaces experimentally, our simulated STM images provide insight into the structures and compositions of the marcasite surfaces, which may otherwise be hard to resolve experimentally, thus explaining why at present no experimental STM images are available for comparison with our results. However, we consider that the simulated STM images may become useful in clarifying future experiments, for instance to distinguish between the {101} and {010} facets, which are the most likely facets to be observed under experimental conditions.

Shown in Fig. 9 are the STM images of the {101} and {010} surfaces with and without adsorbed water molecules. The STM image of the dehydrated {101} surface (Fig. 9a), acquired at a distance (d) of 2.10 Å to the tip and at a density (ρ) of 0.007 e Å⁻³ clearly shows the terminating S dimers as bright spots. The coordinating Fe ions from the layer below are also well-defined circles in rows. The adsorbed water molecules on the {101} surface are highlighted in Fig. 9b. Similarly, the row of S ions terminating the {010} surface are shown as bright spots (Fig. 9c) and the adsorbed water molecules are highlighted in Fig. 9d.

3.4.3 Surface electronic properties. We now discuss the electronic properties of the most stable termination of each marcasite surface. First, we calculated the average charge on Fe and S ions of the fully relaxed most stable terminations of each

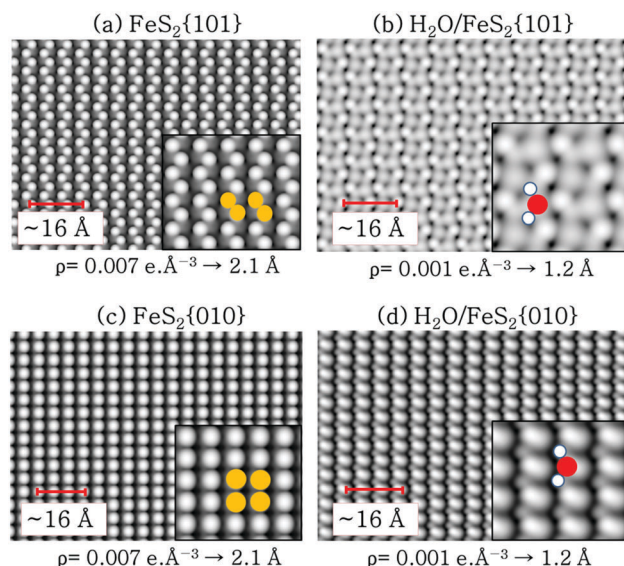


Fig. 9 Simulated STM images of the dehydrated (left) and hydrated (right) of FeS₂{101}–S and FeS₂{010}–S surfaces, obtained using a bias of -2.5 eV. Density (ρ) and tip distance (d) are also indicated. Insets show enlargements of the STM images. In the inset, surface terminating S ions are in yellow, O ions are in red and H ions are in white.

Table 6 Average charge (q) of relaxed topmost surface Fe and S ions and variance with respect to the bulk ions (Δq). The values in round brackets are for the hydrated surfaces

	Fe		S	
	q/e^-	$\Delta q/e^-$	q/e^-	$\Delta q/e^-$
Bulk	0.88		-0.44	
{010}-S	0.89 (0.92)	-0.01 (-0.04)	-0.45 (0.46)	-0.01 (-0.02)
{101}-S	0.87 (0.91)	0.01 (-0.03)	-0.44 (0.46)	0.00 (-0.02)
{110}-S	0.91 (0.93)	-0.03 (-0.05)	-0.46 (0.47)	-0.02 (-0.03)
{130}-S	0.93 (0.96)	-0.05 (0.08)	-0.46 (0.48)	-0.02 (-0.04)

surface before and after hydration, using the Bader charge partition scheme.¹⁰⁰ The results are summarized in Table 6 and are compared with the Fe and S charges in the bulk mineral. Relative to the charges of bulk Fe (+0.88 e^-) and S (-0.44 e^-) charges, each surface Fe ions loses electrons, suggesting slight oxidation toward Fe^{3+} , while S ions gain extra electrons from their neighbouring Fe ions (Δq in Table 6). Similar Bader charges have been calculated for Fe (+0.86 e^-) and S (-0.43 e^-) ions in pyrite.¹⁰¹ Upon hydration, we observed further oxidation of the surface Fe ions as they become more positively charged due to charge transfer to the adsorbed water molecules. The hybridization between the O p-states of the water molecules and the interacting surface species is revealed by the project density of states (PDOS) analysis, as shown in Fig. 10(a2 and b2). Compared to the clean surfaces (Fig. 10(a1 and b1)), we observe reduction of the interacting Fe-d valence states around the Fermi level for the water-covered surfaces, which is consistent with the loss of electrons and the slight oxidation toward Fe^{3+} predicted by the Bader charge analysis. The electron density redistribution (differential electron density iso-surface) within the water-FeS₂ systems due to the newly formed bonds at the {101}-S and {010}-S surfaces, is shown as insets in Fig. 10(a2 and b2).

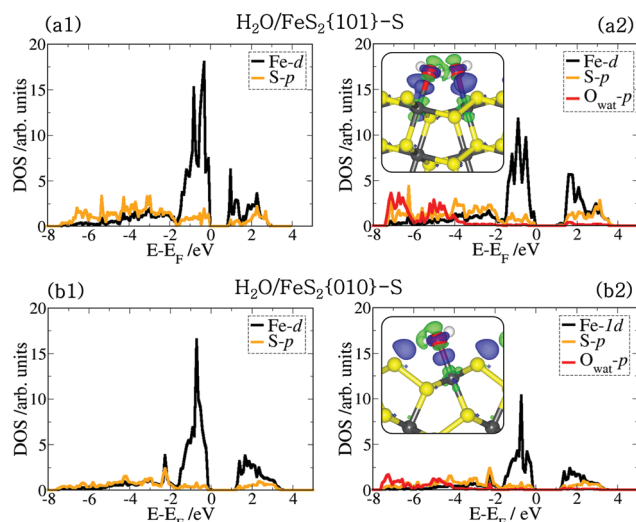


Fig. 10 Projected density of states of the clean (left) and water covered (right) {101}-S and {010}-S surfaces. The insets in the right panel show the corresponding electron density difference iso-surface contours upon water adsorption, where the blue and green contours indicate electron density increase and decrease by 0.02 $e^- \text{ \AA}^{-3}$, respectively.

Table 7 Calculated work functions of the dry (Φ_{dry}) and hydrated (Φ_{hyd}) FeS₂ surfaces

Surface	Φ_{dry} (eV)	Φ_{hyd} (eV)
{010}-S	4.41	3.84
{101}-S	5.10	4.29
{101}-Fe	4.29	3.78
{130}-S	4.52	4.26
{130}-Fe	4.32	4.16
{110}-S	5.32	5.12
{110}-Fe	5.04	4.73

The iso-surface contours reveal electron density accumulation within the bonding regions, which is consistent with the formation of new Fe-O bonds (chemisorption). We also see electron density accumulation between the hydrogen and sulfur atoms, indicative of hydrogen-bonded interactions, which contribute to the stabilization of the water molecules on the surface.

We have also calculated the work function (Φ) of each surface of marcasite before and after hydration, as summarized in Table 7. The work function, which is the minimum energy needed to remove an electron from the bulk of a material through a surface to a point outside the material, is one of the most fundamental parameters of surfaces, and is important to understand a wide range of physical phenomena, such as adsorption, catalytic activity, photoemission and thermionic emission processes. It was calculated as follows:

$$\Phi = V_{\text{vacuum}} - E_F \quad (8)$$

The potential in the vacuum region (V_{vacuum}) and the Fermi energy (E_F) were derived from the same calculation. In practice, this is the energy required at 0 K to remove an electron from the Fermi level of the material to the vacuum potential.¹⁰² We applied dipole corrections perpendicular to all surfaces in the calculations to ensure that there is no net charge or dipole perpendicular to the surfaces, that may affect the potential in the vacuum level. From the results presented in Table 7, we note that the work functions depend on the crystallographic orientation of the surface, a phenomenon known as the anisotropy of the work function.¹⁰³ The work function anisotropy can be understood as a surface effect, *i.e.* the work necessary to take an electron from inside the material to a region outside depends on the surface orientation, since the potential difference between the material and the vacuum is sensitively controlled by the spreading of the electronic charge into the vacuum. This spreading is in turn dependent on the crystallographic arrangement in the surface plane, *i.e.* on the surface orientation.^{103–105} The calculated work functions (4.41–5.34 eV) for the dehydrated surfaces compare well with the value of 5.0 eV obtained from ultraviolet photoelectron spectroscopy (UPS) measurements for the pyrite {100} surface.^{11,106} The work function of the hydrated surfaces is lowered due to partial transfer of electron charge from the substrate to the adsorbate and the resulting adsorption-induced surface dipoles (Table 7).^{107–109} Furthermore, the adsorption acts to smoothen the surface electric charge distribution (the Smoluchowski effect) which lowers the work function.^{110,111}

4. Summary and conclusions

We have performed systematic density functional theory calculations, with Hubbard U corrections (DFT+ U), to provide fundamental insight into the bulk and surface properties of marcasite FeS_2 . From this study, we conclude that marcasite is an indirect band gap semiconductor with a band gap of 1.17 eV, which is slightly larger than the band gap of pyrite (0.95 eV). We have shown from the calculated single-crystal elastic constants that marcasite is mechanically stable at ambient conditions and that the mineral is prone to shear deformation rather than compressive deformation. The Wulff constructed equilibrium morphology shows that $\{101\}$ and $\{010\}$ surfaces dominate the marcasite crystal under both dehydrated and hydrated conditions, in agreement with their relative stabilities compared to the other surfaces. Hydration of the marcasite surfaces acts to coordinate water to the under-coordinated surface Fe ions and so stabilize the surfaces. The large expression of the $\{101\}$ and $\{010\}$ facets in the marcasite crystal morphology compared to the $\{100\}$ facet in the cubic crystal of pyrite,^{112,113} suggests that intergrowth (epitaxial growth) of marcasite with pyrite will most likely occur through the formation of $m\{101\}$ – $p\{100\}$ or $m\{010\}$ – $p\{100\}$ interfaces. The simulated scanning tunneling microscopy (STM) images of the $\{101\}$ and $\{010\}$ facets are also presented, for comparison with future experiments. Our calculations suggest that contrary to earlier speculations, marcasite might actually be a useful semiconductor and photocatalyst in its own right, similar to pyrite.

Conflicts of interest

There are no conflicts to declare.

Acknowledgements

We acknowledge the Netherlands Organisation for Scientific Research (NWO) for funding (Grant No. 13CO26-2). This work made use of the facilities of ARCHER (<http://www.archer.ac.uk>), the UK's national supercomputing service via our membership of the UK's HEC Materials Chemistry Consortium, which is funded by EPSRC (EP/L000202).

References

- D. Rickard and G. W. Luther, *Chem. Rev.*, 2007, **107**, 514–562.
- M. S. Schmøkel, L. Bjerg, S. Cenedese, M. R. V. Jørgensen, Y.-S. Chen, J. Overgaard and B. B. Iversen, *Chem. Sci.*, 2014, **5**, 1408–1421.
- S. Nakamura and A. Yamamoto, *Sol. Energy Mater. Sol. Cells*, 2001, **65**, 79–85.
- Y. Bi, Y. Yuan, C. L. Exstrom, S. A. Darveau and J. Huang, *Nano Lett.*, 2011, **11**, 4953–4957.
- M. A. Khan, J. C. Sarker, S. Lee, S. C. Mangham and M. O. Manasreh, *Mater. Chem. Phys.*, 2014, **148**, 1022–1028.
- S. C. Mangham, M. A. Khan, M. Benamara and M. O. Manasreh, *Mater. Lett.*, 2013, **97**, 144–147.
- J. Puthussery, S. Seefeld, N. Berry, M. Gibbs and M. Law, *J. Am. Chem. Soc.*, 2011, **133**, 716–719.
- P. Namanu, M. Jayalakshmi and K. U. Bhat, *J. Mater. Sci.: Mater. Electron.*, 2015, **26**, 8534–8539.
- H. A. Macpherson and C. R. Stoldt, *ACS Nano*, 2012, **6**, 8940–8949.
- P. Kush, N. C. Mehra and S. Deka, *Sci. Adv. Mater.*, 2013, **5**, 788–795.
- A. Ennaoui, S. Fiechter, C. Pettenkofer, N. Alonso-Vante, K. Büker, M. Bronold, C. Höpfner and H. Tributsch, *Sol. Energy Mater. Sol. Cells*, 1993, **29**, 289–370.
- R. Murphy and D. R. Strongin, *Surf. Sci. Rep.*, 2009, **64**, 1–45.
- C. Wadia, Y. Wu, S. Gul, S. K. Volkman, J. Guo and A. P. Alivisatos, *Chem. Mater.*, 2009, **21**, 2568–2570.
- D. Spagnoli, K. Refson, K. Wright and J. D. Gale, *Phys. Rev. B: Condens. Matter Mater. Phys.*, 2010, **81**, 094106.
- M. S. Jagadeesh and M. S. Seehra, *Phys. Lett. A*, 1980, **80**, 59.
- R. Sun, M. K. Y. Chan and G. Ceder, *Phys. Rev. B: Condens. Matter Mater. Phys.*, 2011, **83**, 235311.
- T. Schena, G. Bihlmayer and S. Blügel, *Phys. Rev. B: Condens. Matter Mater. Phys.*, 2013, **88**, 235203.
- V. K. Gudelli, V. Kanchana, S. Appalakondaiah, G. Vaitheeswaran and M. C. Valsakumar, *J. Phys. Chem. C*, 2013, **117**, 21120.
- S. Seefeld, M. Limpinsel, Y. Liu, N. Farhi, A. Weber, Y. Zhang, N. Berry, Y. J. Kwon, C. L. Perkins, J. C. Hemminger, R. Wu and M. Law, *J. Am. Chem. Soc.*, 2013, **135**, 4412.
- L. Wu, N. Y. Dzade, L. Gao, D. O. Scanlon, Z. Öztürk, N. Hollingsworth, B. M. Weckhuysen, E. J. M. Hensen, N. H. de Leeuw and J. P. Hofmann, *Adv. Mater.*, 2016, **28**, 9602–9607.
- C. Sánchez, E. Flores, M. Barawi, J. M. Clamagirand, J. R. Ares and I. J. Ferrer, *Solid State Commun.*, 2016, **230**, 20–24.
- A. Selloni, *Nat. Mater.*, 2008, **7**, 613–615.
- G. A. Somorjai and Y. Li, *Proc. Natl. Acad. Sci. U. S. A.*, 2011, **108**, 917.
- J. K. Nørskov, T. Bligaard, J. Rossmeisl and C. H. Christensen, *Nat. Chem.*, 2009, **1**, 37–46.
- S. Liu, Y. Li, J. Yang, H. Tian, B. Zhu and Y. Shi, *Phys. Chem. Miner.*, 2014, **41**, 189–196.
- M. Reich and U. Becker, *Chem. Geol.*, 2006, **225**, 278–290.
- E. C. Dos Santos, J. C. de Mendonça Silva and H. A. Duarte, *J. Phys. Chem. C*, 2016, **120**, 2760–2768.
- J. Hu, Y. Zhang, M. Law and R. Wu, *Phys. Rev. B: Condens. Matter Mater. Phys.*, 2012, **85**, 085203.
- A. Stirling, M. Bernasconi and M. Parrinello, *J. Chem. Phys.*, 2003, **118**, 8917.
- P. H.-L. Sit, M. H. Cohen and A. Selloni, *J. Phys. Chem. Lett.*, 2012, **3**, 2409–2414.
- N. H. de Leeuw, S. C. Parker, H. M. Sithole and P. E. Ngoepe, *J. Phys. Chem. B*, 2000, **104**, 7969–7976.
- H. W. Nesbitt and I. J. Muir, *Geochim. Cosmochim. Acta*, 1994, **58**, 4667–4679.
- J. M. Guevremont, D. R. Strongin and M. A. A. Schoonen, *Langmuir*, 1998, **14**, 1361–1366.

- 34 C. M. Eggleston, J. J. Ehrhardt and W. Stumm, *Am. Mineral.*, 1996, **81**, 1036–1056.
- 35 N. Y. Dzade, A. Roldan and N. H. de Leeuw, *J. Chem. Phys.*, 2016, **144**, 174704.
- 36 N. Y. Dzade, A. Roldan and N. H. de Leeuw, *J. Phys. Chem. C*, 2016, **120**, 21441–21450.
- 37 D. Santos-Carballal, A. Roldan and N. H. de Leeuw, *J. Phys. Chem. C*, 2016, **120**(16), 8616–8629.
- 38 A. Roldan and N. H. de Leeuw, *Proc. R. Soc. A*, 2016, **472**, 20160080.
- 39 S. Haider, A. Roldan and N. H. de Leeuw, *J. Phys. Chem. C*, 2014, **118**, 1958–1967.
- 40 G. Wulff, *Z. Kristallogr. Mineral.*, 1901, **34**, 449.
- 41 D. E. P. Vanpoucke and G. Brocks, *Phys. Rev. B: Condens. Matter Mater. Phys.*, 2008, **77**, 241308.
- 42 G. Kresse and J. Hafner, *Phys. Rev. B: Condens. Matter Mater. Phys.*, 1993, **47**, 558–561.
- 43 G. Kresse and D. Joubert, *Phys. Rev. B: Condens. Matter Mater. Phys.*, 1999, **59**, 1758.
- 44 G. Kresse and J. Furthmüller, *Phys. Rev. B: Condens. Matter Mater. Phys.*, 1996, **54**, 11169.
- 45 G. Kresse and J. Furthmüller, *Comput. Mater. Sci.*, 1996, **6**, 15.
- 46 P. E. Blöchl, *Phys. Rev. B: Condens. Matter Mater. Phys.*, 1994, **50**, 17953.
- 47 J. P. Perdew, K. Burke and M. Ernzerhof, *Phys. Rev. Lett.*, 1997, **78**, 1396.
- 48 J. P. Perdew, K. Burke and M. Ernzerhof, *Phys. Rev. Lett.*, 1996, **77**, 3865–3868.
- 49 A. Rohrbach, J. Hafner and G. Kresse, *J. Phys.: Condens. Matter*, 2003, **15**, 979.
- 50 B. Himmetoglu, A. Floris, S. de Gironcoli and M. Cococcioni, *Int. J. Quantum Chem.*, 2014, **114**, 14–49.
- 51 V. I. Anisimov, F. Aryasetiawan and A. I. Lichtenstein, *J. Phys.: Condens. Matter*, 1997, **9**, 767.
- 52 J. Hu, Y. Zhang, M. Law and R. Wu, *J. Am. Chem. Soc.*, 2012, **134**, 13216–13219.
- 53 P. Xiao, X.-L. Fan, L.-M. Liu and W.-M. Lau, *Phys. Chem. Chem. Phys.*, 2014, **16**, 24466–24472.
- 54 J. Hu, Y. Zhang, M. Law and R. Wu, *Phys. Rev. B: Condens. Matter Mater. Phys.*, 2012, **85**, 085203.
- 55 S. Grimme, J. Antony, S. Ehrlich and S. Krieg, *J. Chem. Phys.*, 2010, **132**, 154104.
- 56 H. J. Monkhorst and J. D. Pack, *Phys. Rev. B: Solid State*, 1976, **13**, 5188.
- 57 Y. Le Page and P. Saxe, *Phys. Rev. B: Condens. Matter Mater. Phys.*, 2002, **65**, 104104.
- 58 A. J. Wang, S. L. Shang, Y. Du, Y. Kong, L. J. Zhang, L. Chen, D. D. Zhao and Z. K. Liu, *Comput. Mater. Sci.*, 2010, **48**, 705–709.
- 59 Q. Gao, Y. Du, D. Zhao, A. Wang, J. Wang, S. Liu and Y. Ouyang, *Calphad*, 2012, **37**, 137–144.
- 60 S. Liu, Y. Li, J. Yang, H. Tian, B. Zhu and Y. Shi, *Phys. Chem. Miner.*, 2014, **41**, 189.
- 61 A. Roldan, D. Santos-Carballal and N. H. de Leeuw, *J. Chem. Phys.*, 2013, **138**, 204712.
- 62 W. Voigt and Lehrbuch der Kristallphysik, *Teubner. Leipzig*, 1928, 1–20.
- 63 Z. Wu, E. Zhao, H. Xiang, X. Hao, X. Liu and J. Meng, *Phys. Rev. B: Condens. Matter Mater. Phys.*, 2007, **76**, 054115.
- 64 G. W. Watson, E. T. Kelsey, N. H. de Leeuw, D. J. Harris and S. C. Parker, *J. Chem. Soc., Faraday Trans.*, 1996, **92**, 433.
- 65 P. W. Tasker, *J. Phys. C: Solid State Phys.*, 1979, **12**, 4977.
- 66 W. R. Tyson and W. A. Miller, *Surf. Sci.*, 1977, **62**, 267.
- 67 R. Stumpf, *Surf. Sci.*, 2007, **601**, L115.
- 68 A. L. Smith, H. M. Shirazi and S. R. Mulligan, *Biochim. Biophys. Acta*, 2002, **1594**, 150–159.
- 69 M. J. Buerger, *Am. Mineral.*, 1931, **16**, 361–395.
- 70 M. J. Buerger, *Z. Kristallogr.*, 1937, **97**, 504–513.
- 71 F. Hulliger and E. Mooser, *J. Phys. Chem. Solids*, 1965, **26**, 429–433.
- 72 G. Brostigen and A. Kjekshus, *Acta Chem. Scand.*, 1970, **24**, 2983–2992.
- 73 M. L. Huggins, *Phys. Rev.*, 1922, **19**, 369–373.
- 74 H. M. Sithole, D. Nguyen-Manh, D. G. Pettifor and P. E. Ngoepe, *Mol. Simul.*, 1999, **22**, 31–37.
- 75 A. Schlegel and P. Wachter, *J. Phys. C: Solid State Phys.*, 1976, **9**, 3363.
- 76 M. Born and K. Huang, *Dynamical Theory of Crystal Lattices*, Oxford University Press, Oxford, UK, 1988.
- 77 T. Chattopadhyay and H. G. von Schnering, *J. Phys. Chem. Solids*, 1985, **46**, 113–116.
- 78 I. R. Shein and A. L. Ivanovskii, *Scr. Mater.*, 2008, **59**, 1099.
- 79 J. Haines, J. M. Leger and G. Bocquillon, *Annu. Rev. Mater. Res.*, 2001, **31**, 1.
- 80 L. Pauling and M. L. Huggins, *Z. Kristallogr.*, 1934, **87**, 205.
- 81 J. A. Tossell, *J. Chem. Phys.*, 1977, **66**, 5712–5719.
- 82 J. A. Tossell, D. J. Vaughan and J. K. Burdett, *Phys. Chem. Miner.*, 1981, **7**, 177–184.
- 83 T. Li, Z. Guo, X. Li, Z. Wu, K. Zhang, H. Liu, H. Sun, Y. Liu and H. Zhang, *RSC Adv.*, 2015, **5**, 98967–98970.
- 84 Miner. Database, <http://webmineral.com/data/Marcasite.shtml#.VxdaPvI96Uk>.
- 85 E. Wasserman, J. R. Rustad, A. R. Felmy, B. P. Hay and J. W. Halley, *Surf. Sci.*, 1997, **385**, 217.
- 86 C. S. Lo, K. S. Tanwar, A. M. Chaka and T. P. Trainor, *Phys. Rev. B: Condens. Matter Mater. Phys.*, 2007, **75**, 075425.
- 87 N. H. de Leeuw and T. G. Cooper, *Geochim. Cosmochim. Acta*, 2007, **71**, 1655.
- 88 N. Y. Dzade, A. Roldan and N. H. de Leeuw, *Minerals*, 2014, **4**, 89–115.
- 89 S. E. Mason, C. R. Iceman, T. P. Trainor and A. M. Chaka, *Phys. Rev. B: Condens. Matter Mater. Phys.*, 2010, **81**, 125423.
- 90 N. H. de Leeuw and S. C. Parker, *J. Phys. Chem. B*, 1998, **102**, 2914–2922.
- 91 E. Osei-Agyemang, J.-F. Paul, R. Lucas, S. Foucaud and S. Cristol, *Phys. Chem. Chem. Phys.*, 2015, **17**, 21401–21413.
- 92 N. Y. Dzade, A. Roldan and N. H. de Leeuw, *Phys. Chem. Chem. Phys.*, 2016, **18**, 32007–32020.
- 93 W. Piskorz, J. Gryboś, F. Zasada, P. Zapala, S. Cristol, P. Jean-François and Z. Sojka, *J. Phys. Chem. C*, 2012, **116**, 19307–19320.

- 94 H. Lee, C. Kim, S. Yang, J. Han and J. Kim, *Catal. Surv. Asia*, 2012, **16**, 14.
- 95 J. G. Che, C. T. Chan, W.-E. Jian and T. C. Leung, *Phys. Rev. B: Condens. Matter Mater. Phys.*, 1998, **57**, 1875–1880.
- 96 T. Madey, J. Guan, C. H. Nien, C. Z. Dong, H. S. Tao and R. A. Campbell, *Surf. Sci. Rev. Lett.*, 1996, **3**, 1315.
- 97 Y. Yin, C. Erdonmez, S. Aloni and A. P. Alivisatos, *J. Am. Chem. Soc.*, 2006, **128**, 12671–12673.
- 98 J. Tersoff and D. R. Hamann, *Phys. Rev. B: Condens. Matter Mater. Phys.*, 1985, **31**, 805–813.
- 99 S. Irrera, A. Roldan, G. Portalone and N. H. de Leeuw, *J. Phys. Chem. C*, 2013, **117**, 3949–3957.
- 100 R. F. W. Bader, *Atoms in Molecules: a Quantum Theory*, Oxford University Press, New York, 1990.
- 101 Y. N. Zhang, J. Hu, M. Law and R. Q. Wu, *Phys. Rev. B: Condens. Matter Mater. Phys.*, 2012, **85**, 085314.
- 102 N. D. Lang and W. Kohn, *Phys. Rev. B: Solid State*, 1971, **3**, 1215.
- 103 C. Fall, *Ab initio study of the work functions of elemental metal crystals*, PhD thesis, École polytechnique fédérale de Lausanne, 1999.
- 104 J. L. F. Da Silva, C. Stampfl and M. Scheffler, *Surf. Sci.*, 2006, **600**, 703.
- 105 J. J. Attema, M. A. Uijttewaalt, G. A. de Wijs and R. A. de Groot, *Phys. Rev. B: Condens. Matter Mater. Phys.*, 2008, **77**, 165109.
- 106 L. Samad, M. Cabán-Acevedo, M. J. Shearer, K. Park, R. J. Hamers and S. Jin, *Chem. Mater.*, 2015, **27**, 3108.
- 107 W. Zhang, L. Liu, L. Wan, L. Liu, L. Cao, F. Xu, J. Zhao and Z. Wu, *Phys. Chem. Chem. Phys.*, 2015, **17**, 20144–20153.
- 108 Y. Ji, Y. Du and M. Wang, *Sci. World J.*, 2014, **2014**, 490853.
- 109 S. H. Chou, J. Voss, I. Bargatin, A. Vojvodic, R. T. Howe and F. Abild-Pedersen, *J. Phys.: Condens. Matter*, 2012, **24**, 445007.
- 110 N. E. Singh-Miller and N. Marzari, *Phys. Rev. B: Condens. Matter Mater. Phys.*, 2009, **80**, 235407.
- 111 R. Smoluchowski, *Phys. Rev.*, 1941, **60**, 661.
- 112 H. Xian, J. Zhu, X. Liang and H. He, *RSC Adv.*, 2016, **6**, 31988–31999.
- 113 L. Zhu, B. J. Richardson, J. Tanumihardja and Q. Yu, *CrystEngComm*, 2012, **14**, 4188–4195.